Title
Identification and compensation of feedthrough in an unstable electrostatic bearing

Authors
Andonian, Michael
M'Closkey, Robert T

Publication Date
2020-02-01

DOI
10.1016/j.mechatronics.2019.102315

Peer reviewed

Identification and compensation of feedthrough in an unstable electrostatic bearing

Michael Andonian, Robert T. M'Closkey*

Mechanical and Aerospace Engineering Department, Samueli School of Engineering and Applied Science, 420 Westwood Plaza, University of California, Los Angeles, CA 90095

Abstract

A technique to identify feedthrough coupling in an unstable one degree-of-freedom electrostatic bearing is described. The feedthrough is caused by the simultaneous use of electrodes for differential capacitive sensing and electrostatic actuation. Cancellation of the feedthrough over a broad frequency band is necessary for the system to be practically stabilizable. A feedforward filter based on open-loop estimates of the feedthrough is adequate for designing a stabilizing controller, however, the resulting stability margins are poor because the closed-loop feedthrough differs from the open-loop estimates which determine the filter. The main contribution of the paper shows how the initial feedforward filter can be updated using feedthrough estimates obtained by testing the closed-loop system at its nominal operating point. It is demonstrated that the improved feedthrough cancellation facilitates the implementation of an updated controller which reduces sensitivity function peaking and increases the closed-loop bandwidth.

1. Introduction

This paper describes the design and implementation of a feedforward filter to improve the closed-loop disturbance rejection properties of an unstable one degree-of-freedom (DOF) electrostatic bearing. A pair of antagonistic electrodes is used to measure the position, and control the motion, of a thin beam as it rotates on a fulcrum situated on a glass substrate. The electrodes are deposited on the glass substrate on opposite sides of the fulcrum. The gaps are changed in a differential manner as the beam rotates. This system is referred to as an electrostatic bearing given its similarities to the electrostatic suspension proposed in [1]. The 1-DOF system is a testbed for developing the transduction scheme, modeling approach, and controller design for a future electrostatically levitated multi-DOF contactless platform. An intended application of this platform is to empirically quantify the dynamics of micro-scale planar resonators by minimizing anchor forces in the suspended resonator. An example of such a resonator is given in [2]. Multiple demonstrations of electrostatically levitated proof masses for accelerometers and gyroscopes have been achieved, eg. [3, 4, 5], and employ some form of differential capacitance sensing to detect motion of the suspended device. One key departure from the aforementioned references is that the electrical interface in this paper relies on using the pair of electrodes as both a capacitive pick-off and an electrostatic forcer. This arrangement reduces the complexity of the electronics and system design, however it naturally produces significant "feedthrough" of the control signal into the measurement that is related to the beam angle. It is necessary to reduce the severity of the feedthrough for two reasons. First, an accurate indication of the beam pose is not possible if the feedthrough of the control signal is left uncompensated. Indeed, it will be shown that the frequency response of the feedthrough has approximately the same magnitude as the beam motional frequency response at low frequencies. Second, the beam-electrical interface forms an unstable system so feedback is necessary to stabilize the beam at a desired angle. However, if left uncompensated, the feedthrough prevents the development of adequate phase lead necessary for stabilizing the system. Thus, if the feedthrough is not cancelled to some degree, the system is not practically stabilizable.

The present paper shows how the identification of a higher fidelity feedthrough model and the implementation of an updated feedforward filter can significantly improve the closed-loop performance over what was achieved in [6]. This reference demonstrated that a feedforward filter identified from *open-loop* measurements can reduce the feedthrough by about an order of magnitude. This level of reduction was adequate for implementing a stabilizing controller, however, the associated stability margins were poor. For example, the magnitudes of the sensitivity and complementary sensitivity functions were reported in [6] to be about 4 from DC to 200 Hz. This high sensitivity is undesirable as it causes amplification of disturbances and noise over a broad frequency band. In order to reduce the closed-loop system's sensitivity function magnitude, improved matching between the feedforward filter and feedthrough dynamics is necessary. Toward this end, the feedforward filter based on open-loop measurements must be updated in the closed-loop system to account for subtle changes in the feedthrough due to stabilizing the beam about a different position. Better matching between the feedforward filter and the actual feedthrough dynamics allows more phase lead within the controller since greater suppression of the feedthrough is achieved. This improves the stability margins and reduces the closed-loop sensitivity function magnitude. Since an improved model of the feedthrough can only be de-

*Corresponding author, Tel.: 00 1 310 825 2909

Email addresses: andonian23@g.ucla.edu (Michael Andonian), rtm@seas.ucla.edu (Robert T. M'Closkey)

termined from closed-loop tests after the initial stabilization of the beam, the procedure is referred to as *bootstrap feedforward compensation*.

The paper is organized as follows. Sec. 2 discusses the fabrication of the beam and substrate as well as the electronics interface to the balanced transformer used for signal transduction. Sec. 3 discusses the stability and approximate frequency response properties of the linear time-varying different equation describing the beam motion about its equilibrium position. The model details and the notion of its frequency response are presented in the Appendices. Experimental results are reported in Sec. 4, and Sec. 5 analyzes the robustness of the feedforward cancellation scheme to errors in the feedthrough models. Sec. 6 concludes the paper.

2. System Description and Setup

2.1. Beam-Substrate Geometry

A thin rectangular beam, 5.2 cm in length and 2.5 cm in width, is etched from a 500 μm thick silicon wafer. The beam is coated with gold to ensure an equipotential body. A 10 μm high fulcrum is created by patterning SU-8 onto a glass substrate. Fabrication details are given in [6]. A pair of gold electrodes is deposited on the substrate with one electrode on each side of the fulcrum. When the beam rests atop the fulcrum and is parallel to the glass below, nominal 10 μm beam-electrode gaps are formed –see Fig. 1. Due to the beam geometry and nominal gaps, only small angular deflections are possible. From the electrode symmetry about the fulcrum, angular deflections of the beam correspond to changes in the beam-electrode gaps by $\pm L\theta$, where L is the length measured normal from the fulcrum to the electrodes' geometric center, and θ represents the beam angle referenced from the parallel with the substrate. The beam is held at ground potential via a wire bond on its topside. A simple parallel plate capacitor model is sufficient for describing the relationship between the beam-electrode gap and capacitance.

2.2. Transducer Description

The block diagram representation of the beam-transformer subsystem coupled with the mixing circuitry and DSP interface is shown in Fig. 1. Collectively, this represents the electromechanical system denoted P. The input, u, and output, y, of P are discrete-time signals generated and acquired, respectively, by the DSP which implements the controller.

The processes involved in producing the plant output y is now described. A transformer is connected to the electrodes by traces that terminate in wire bond pads as indicated in the Fig. 1 schematic. The transformer consists of two primary windings, with equal inductances, connected via a center tap. The center tap is driven by a current source that supplies a sinusoidal current $i_{ct}(t) = a_{ct}\cos(2\pi\omega_0 t)$, where a_{ct} is the (constant) amplitude and ω_0 is the carrier frequency. The center tap current establishes the master phase against which all other steady-state sinusoidal signals are referenced. By maintaining the beam at ground potential, the current delivered to each electrode is largely unaffected by the beam-electrode capacitances, denoted C_1 and C_2, because of the large primary inductances. Thus, the potential between the beam and an electrode is essentially determined by its capacitance. Beam deflection from parallel creates a differential change in the capacitances which produces a differential change in the electrode potentials as shown in Fig. 2. The coupling between the transformer primary and secondary induces a sinusoidal voltage drop $v_s(t) = a_s(t)\cos(2\pi\omega_0 t + \phi_s)$ across the secondary windings. Thus, the transformer acts as a differential capacitance transducer and the amplitude a_s effectively represents a measurement of the beam deflection θ relative to the "balanced" condition when $C_1 = C_2$. Demodulation of the v_s signal with a phase-synchronized signal $\cos(2\pi\omega_0 t + \phi_s)$ yields a measurement of a_s and enables tracking of the beam motion. The filter H_a eliminates the $2\omega_0$ component in $v_s(t)\cos(2\pi\omega_0 t + \phi_s)$ and also acts as an anti-alias filter prior to sampling by the ADC. The phase ϕ_s is simply chosen to be in-phase with the voltage created at v_s when $\theta > 0$ –this phase is easily determined by open loop testing of the unstabilized beam.

The transformer also offers an avenue for exerting controlled electrostatic forces on the beam. Through resistor R_k in series with the transformer secondary load, the control potential, defined as $v_c(t) = a_c(t)\cos(2\pi\omega_0 t + \phi_c)$, induces a differential sinusoidal potential on each electrode, i.e., electrode potentials arising from v_c invariably have a 180° phase difference due to the magnetic coupling within the transformer windings. In contrast, the i_{ct}-induced potentials on both electrodes are in-phase with one another. Note that the superposed effects of i_{ct} and v_c are sinusoidal with frequency ω_0. The phase of the control signal ϕ_c is therefore selected so the v_c-induced component on one of electrodes is in-phase with the i_{ct}-induced voltage and therefore the v_c-induced component of the remaining electrode is anti-phase with the i_{ct}-induced component. With ϕ_c chosen in this manner and the center tap current applied, then $a_c \neq 0$ produces a *differential* change in the *amplitudes* of the two electrode voltages (see Fig. 2). Because the electrostatic forces are proportional to the square of the electrode voltages, this differential change in the amplitudes produces the largest moment on the beam for a given value of a_c. Note that a_c is the smoothed output of the controller: the discrete-time controller output is extended by a zero-order hold and then passed through the smoothing filter H_s.

3. Control-oriented model

Equations of motion for the beam-transformer subsystem can be determined from first principles and augmented to include the modulation, demodulation, and filtering stages. This resulting set of equations is overdetermined and nonlinear, nevertheless, a periodic solution exists in which the beam is in equilibrium. Thus, the linear variational equations are determined about this solution. This analysis and the reduction to the essential states is given in Appendix A where the following model is generated,

$$\begin{aligned} \dot{\delta} &= A_\delta(t)\delta + B_\delta(t)u \\ y &= C_\delta\delta \end{aligned} \tag{1}$$

Both A_δ and B_δ are time-periodic with period $\tau_p = 1/\omega_0$ and the state dimension is 20 for the system under study. The state

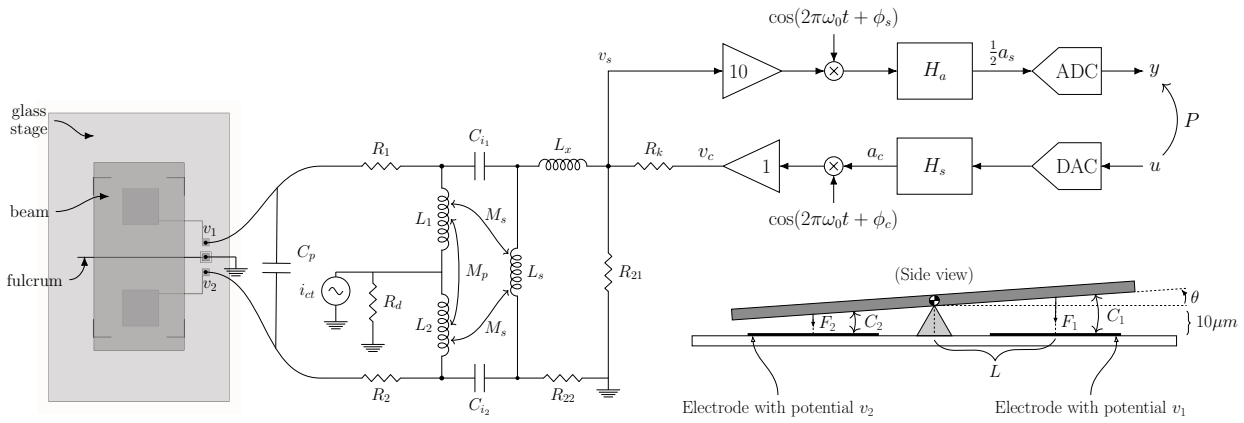

Figure 1: Schematic of beam-transformer system including the signal conditioning for plant control and measurement. Side view of the beam relative to electrodes is not to scale.

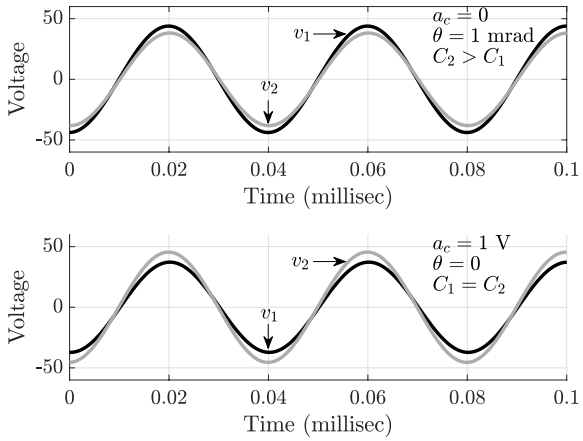

Figure 2: Electrode potentials v_1 and v_2 when $v_c = 0$ and $C_2 > C_1$ (top), and when $v_c \neq 0$ and $C_2 = C_1$ (bottom).

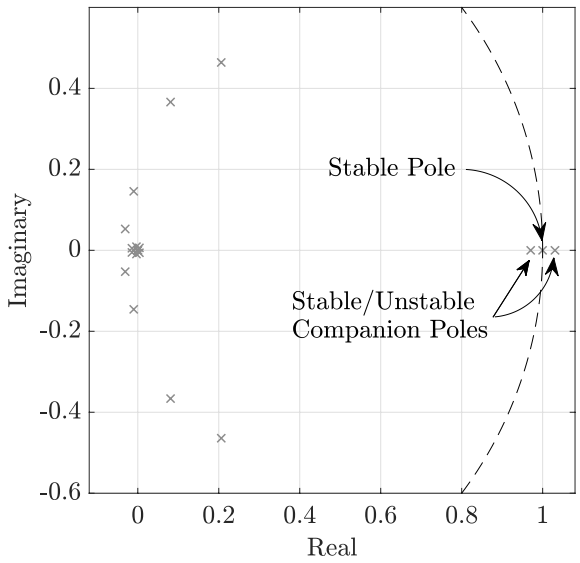

Figure 3: Characteristic multipliers associated with time-periodic model. There is one unstable characteristic multiplier.

transition matrix is denoted $\Phi(t, t_0)$ for this periodic system. Stability of the periodic solution corresponding to the beam in equilibrium and parallel to the substrate is determined by analyzing the system's characteristic multipliers, which are the eigenvalues of $\Phi(\tau_p, 0)$. The characteristic multipliers are shown in Fig. 3 when $\omega_0 = 25$ kHz, $a_{ct} = 2.3$ mA, the nominal electrode capacitances are $C_1 = C_2 = 107$ pF, and with the transformer and beam parameters defined in Table. A.1. Numerical integration of (1) is used to estimate $\Phi(\tau_p, 0)$. The system is unstable due the single characteristic multiplier outside the unit disk. The continuous-time representation of the unstable characteristic multiplier and its companion multiplier correspond to real poles at approximately ± 119Hz. A scenario exists in which the C_1 and C_2 capacitors are charged even if $i_{ct} = 0$ and $v_c = 0$. Constant potentials on the transformer primary develop as a result and all other currents and potentials are zero. This mode in the circuit equations (A.1) maps to a characteristic multiplier on the unit circle. In practice, however, the current source supplying i_{ct} has a parasitic resistance to ground which is modeled by R_d as shown in Fig. 1. This pulls the characteristic multiplier slightly inside the unit circle and has a continuous-time real pole representation of approximately -2.8 rad/s. Thus, $I - \Phi(\tau_p, 0)$ is invertible, which is a condition that is assumed in the frequency response analysis given in Appendix B.

Classical loop-shaping techniques are used to synthesize stabilizing controllers. Consequently, it is necessary to have a frequency response representation of the plant [7]. Since (1) is time-periodic its frequency response does not exist in a strict sense. Nevertheless, Appendix B describes a method to generate the approximate frequency response shown in Fig. 4 that predicts the measurements in Section 4 with remarkable accuracy (compare to Fig. 9). The *feedthrough* from plant input to plant output is quite evident above 200 Hz in y/u. Its magnitude is essentially constant from DC to 10 kHz so the increase in magnitude that occurs for frequencies below 200 Hz is due to the motional signal of the beam in addition to the feedthrough. The model can be

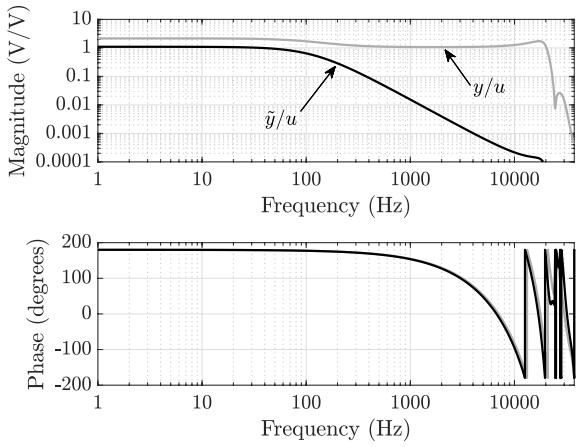

Figure 4: Frequency response estimate of the discrete-time plant model P with feedthrough (y/u), and with feedthrough removed ($\tilde{y}/u$).

manipulated to exhibit only the feedthrough dynamics by setting the electrode capacitances to be constant and equal (removing the beam dynamics) and then computing the frequency response of this modified model. Then, the beam's motional frequency response is obtained by subtracting the feedthrough frequency response from the full model frequency response –the motional response is the trace labeled $\tilde{y}/u$ in Fig. 4. Note that the unstable beam response is essentially a low-pass filter with corner frequency near 119 Hz. This corner frequency is consistent with the stable and unstable companion poles computed from the eigenvalues of $\Phi(\tau_p, 0)$. The -40 dB per decade slope above the corner frequency is also consistent with this pair of poles. In practice, it is not possible stabilize the beam without first reducing the feedthrough contribution in the measurement: the feedthrough summed with the unstable system representing the beam motional response essentially creates an unstable transfer function zero that is in close proximity to the unstable pole –this is why the magnitude of y/u in Fig. 4 is essentially constant. Systems with near unstable pole-zero cancellations necessarily have large ($>> 1$) maximum magnitudes of the sensitivity and complementary functions and are therefore difficult to robustly stabilize [7].

4. Experimental results

The experiments are performed with the following parameters: $a_{ct} = 2.65$ mA, $\omega_0 = 25$ kHz, sampling frequency $\omega_s = 75$ kHz, H_s is a 4-pole low-pass Butterworth filter with 20 kHz corner frequency, and H_a is an 8-pole low-pass Butterworth filter with 20 kHz corner frequency. The beam and glass substrate reside in a vacuum chamber maintained at a pressure of approximately 10 μTorr. The vacuum is necessary in order to remove squeeze film damping between the beam and substrate. The electronics are located outside the vacuum chamber along with the DSP. Fig. 5 illustrates the signals and dynamic blocks: K is the discrete-time controller, P is the discrete-time plant (refer to model frequency response in Fig. 4), H_f is the initial feedforward filter transfer function, and H_b is the bootstrap feedforward filter transfer function.

4.1. Initial feedforward filter

An estimate of the feedthrough must be obtained prior to stabilizing the beam. The initial feedthrough estimate is obtained from open-loop measurements by simply correlating y with u when u is a white stationary sequence (constant power spectral density from DC to the Nyquist frequency). In open-loop, the beam rests at its maximum deflection angle on the fulcrum with one edge in contact with the glass substrate. A lower threshold of the moment created by the electrostatic forces must be exceeded to lift the beam edge that rests on the substrate, thus, the amplitude of the plant input u is limited so as to not induce beam motion. Furthermore, the controller is zero for this test, i.e. $K = 0$, so the test input is supplied by the signal d which is injected at the plant input ($u = d$ in open-loop). Consequently, measurement of the transfer function y/u represents the feedthrough due to the transformer dynamics established by the specific electrode capacitances created by the beam in this resting pose.

The time-domain impulse response of the initial feedforward filter, denoted h_f, is implemented as a finite impulse response (FIR) filter. The filter taps are specified to be the first 60 terms of the empirical impulse response of the feedthrough as measured in the aforementioned test. The filter taps are shown in Fig. 6. Compared to other filter realizations, the FIR form of the feedforward filter provided superior feedthrough cancellation. In fact, the efficacy of the filter in cancelling the feedthrough is evident in Fig. 7 which shows the empirical frequency responses obtained via open-loop testing of the system. The graph labeled y/u is simply the feedthrough existing in the system with the beam at its rest pose, and the graph labeled $\tilde{y}/u$ represents the *compensated* plant output with feedthrough "cancelled" by the feedforward filter h_f (in Fig. 5, the second feedforward filter, H_b, has transfer function equal to 1). Fig. 7 demonstrates that feedthrough in the compensated output has been suppressed by a factor of 100 from DC to 10 kHz, and even above 10 kHz the suppression is at least a factor of 20. These cancellation results, however, are achieved in the open-loop system.

Stabilizing the beam about a reference angle with a feedback controller is only achievable with the initial feedforward filter h_f in place (with $H_b = 1$). Based on the frequency response estimated from the model with the feedthrough removed ($\tilde{y}/u$ in Fig. 4) and the uncertainty associated with the level of feedthrough cancellation that is achieved in the closed-loop system, the low-gain phase-lead filter denoted K_1 in Fig. 8 is used to initially stabilize the beam. A notch filter near 2 kHz was added to the controller to compensate a lightly damped beam flexural mode that is present when the beam is operated in a vacuum. Although it is clear that K_1 provides some phase lead, it is relatively weak because the magnitude of K_1 is limited at frequencies greater than a few hundred hertz.

Scaling the magnitude of K_1 beyond what is shown in Fig. 8 did not produce a stable closed-loop system. This behavior appears contradictory given the 40 dB reduction in feedthrough that was achieved in the open-loop system. To understand the

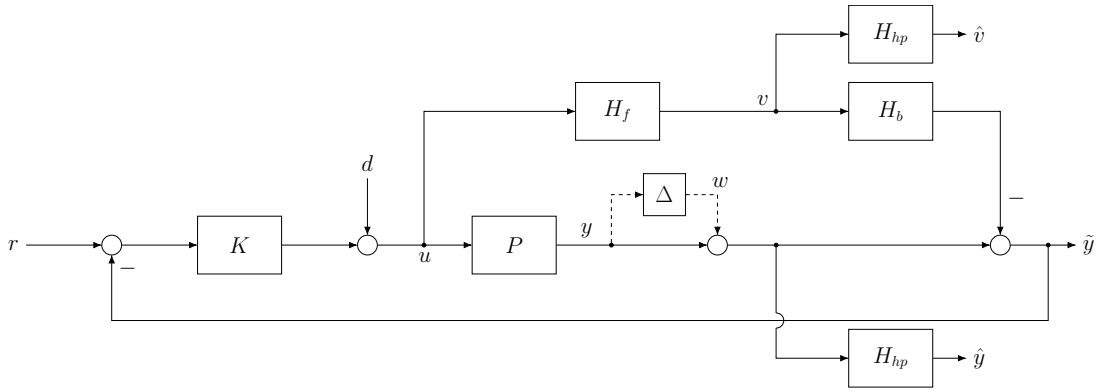

Figure 5: Block diagram of the closed-loop system including the feedforward compensation. The input sensitivity function u/d is used a measure of system performance.

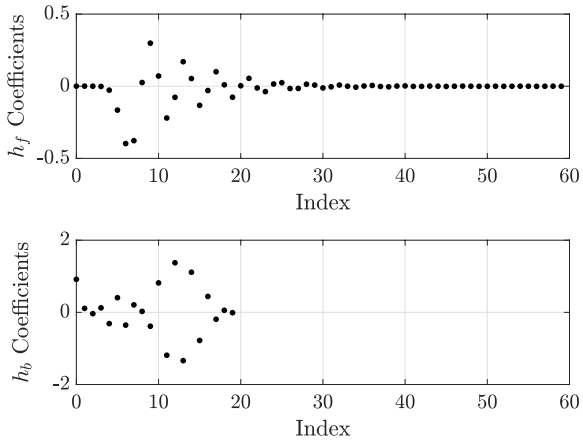

Figure 6: Filter coefficients for h_f (top) and h_b (bottom) where $\sum_k h_b[k] = 0.999$.

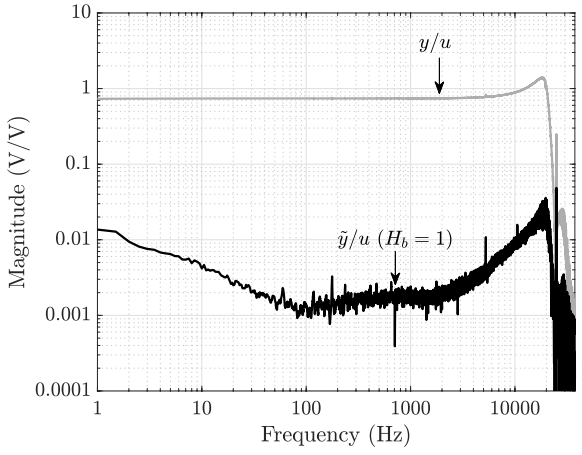

Figure 7: Open-loop empirical frequency responses y/u and $\tilde{y}/u$. The compensated frequency response $\tilde{y}/u$ is determined using the FIR feedforward filter h_f given in Fig. 6.

cause, it is necessary to measure the open-loop response of the feedthrough-compensated plant. It is possible to identify the open-loop plant frequency response about its nominal operating point by testing the *stabilized* system. In this case, the two closed-loop frequency responses $\tilde{y}/d$ and u/d are measured relative to the external stimulus d, then, the open-loop frequency response is estimated as $\tilde{y}/u = (\tilde{y}/d)(u/d)^{-1}$. The cause of the gain limitation is revealed in Fig. 9: when the beam is stabilized and the electrode capacitances are essentially equal, the feedthrough dynamics have changed from model that was obtained by open-loop testing. Comparing the residual feedthrough in Figs. 7 and 9 shows that the cancellation of the feedthrough in the stabilized system is, in fact, much poorer at higher frequencies. The result is a relatively large input sensitivity function u/d, denoted S_1 in Fig. 10. Nevertheless, Fig. 9 clearly reveals the motional response of the beam in the frequency response of the feedthrough-compensated plant, i.e. $\tilde{y}/u$. Also shown is a frequency response estimate of the uncompensated plant, y/u. Agreement with the *model* frequency responses in Fig. 4 is excellent and lends further confidence to the approximate frequency response analysis discussed in Appendix B.

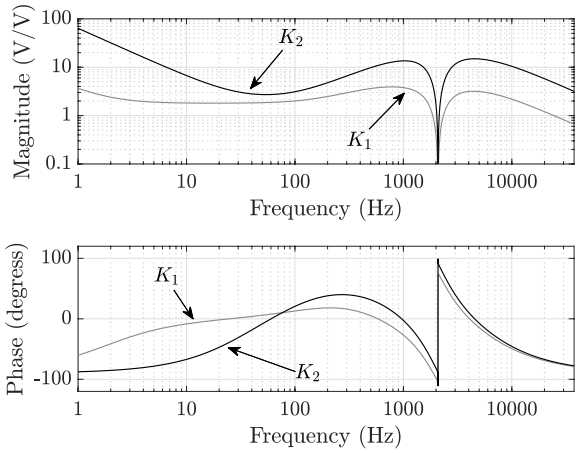

Figure 8: The controller K_1 is used to initially stabilize the beam, however, the maximum input sensitivity magnitude is too large (see Fig. 10). Better cancellation of the plant feedthrough permits the implementation of K_2.

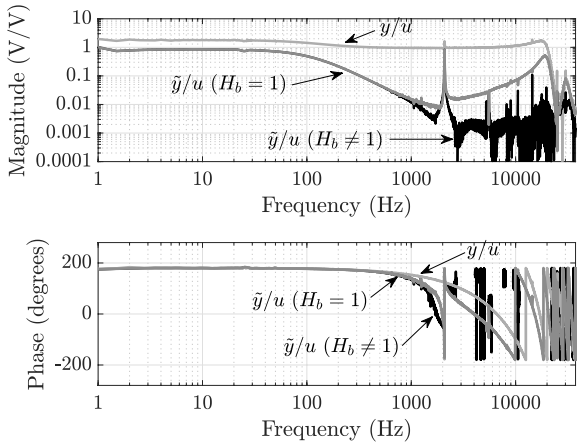

Figure 9: Open-loop frequency response estimates of y/u and $\tilde{y}/u$ obtained from testing the stabilized beam. The compensated plant response $\tilde{y}/u$ is shown with $H_b = 1$ and also with an updated filter $H_b \neq 1$. Improved high-frequency attenuation of the feedthrough is achieved with the updated filter.

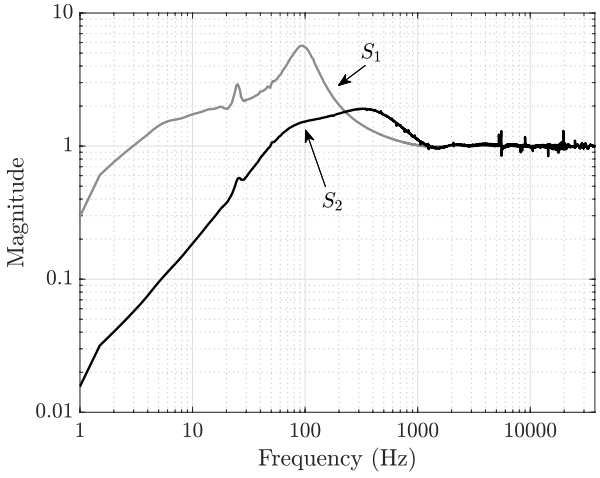

Figure 10: Measured input sensitivity functions associated with the controllers and feedforward schemes.

4.2. Bootstrap Feedforward Filter

The impediment to decreasing the input sensitivity function magnitude is due to the limited controller gain which is a consequence of the incomplete cancellation of the feedthrough that manifested when the beam was stabilized. Thus, the issue is one of improving the feedthrough cancellation based on measurements of the stabilized system. The cancellation need only be improved beyond 1 kHz, however, because of the phase-lead nature of the controller. The motional response of the beam is greatly attenuated above 1 kHz, so by comparing y to v (refer to Fig. 5 for v) in closed-loop for frequencies greater than 1 kHz, the deficiencies in the ability of h_f to model the feedthrough will be revealed. In practice, this is achieved by filtering the closed-loop signals v and y with identical high-pass filters, denoted H_{hp}, to produce the signals $\hat{v}$ and $\hat{y}$. The outputs of the high-pass filters are correlated with the broadband stimulus d to produce the cross-correlation functions $R_{\hat{y}d}$ and $R_{\hat{v}d}$. Any difference between $R_{\hat{y}d}$ and $R_{\hat{v}d}$ can be attributed to the imperfect modeling of the feedthrough by h_f since the corner frequency of H_{hp} is chosen so that any motional signals are filtered out. It is possible to determine a correction to the feedforward filter by searching for a causal filter, whose impulse response is given by h_b, such that $R_{\hat{y}d} = h_b * R_{\hat{v}d}$, where $*$ denotes convolution. The filter h_b can be determined only after the system has been stabilized about its nominal operating point. Note that h_b appears in series with the original feedforward filter h_f as shown in Fig. 5. The frequency response of h_b is denoted H_b.

Since $R_{\hat{v}d}$ is not impulsive, h_b is determined from a least-squares problem. It is assumed that h_b is also an FIR filter with q taps. The least-squares problem is formulated as

$$\min_{\vec{h}_b} \ \|\vec{R}_{\hat{y}d} - \tilde{R}_{\hat{v}d}\vec{h}_b\|_2^2 + \gamma(1 - \mathbf{1}\vec{h}_b)^2, \tag{2}$$

where $\vec{h}_b \in \mathbf{R}^q$ is the vector of impulse response samples of h_b and $\vec{R}_{\hat{y}d} \in \mathbf{R}^p$ is the vector cross-correlation values,

$$\vec{h}_b = \begin{bmatrix} h_b[0] \\ h_b[1] \\ \vdots \\ h_b[q-1] \end{bmatrix}, \quad \vec{R}_{\hat{y}d} = \begin{bmatrix} R_{\hat{y}d}[0] \\ R_{\hat{y}d}[1] \\ \vdots \\ R_{\hat{y}d}[p-1] \end{bmatrix},$$

and $\tilde{R}_{\hat{v}d} \in \mathbf{R}^{p\times q}$ is a Toeplitz matrix of cross-correlation values,

$$\tilde{R}_{\hat{v}d} = \begin{bmatrix} R_{\hat{v}d}[0] & 0 & \cdots & 0 \\ R_{\hat{v}d}[1] & R_{\hat{v}d}[0] & \cdots & 0 \\ \vdots & \vdots & \ddots & \vdots \\ R_{\hat{v}d}[q-1] & R_{\hat{v}d}[q-2] & \cdots & R_{\hat{v}d}[0] \\ \vdots & \vdots & \vdots & \vdots \\ R_{\hat{v}d}[p-1] & R_{\hat{v}d}[p-2] & \cdots & R_{\hat{v}d}[p-1-q] \end{bmatrix}$$

It is assumed $p > q$. Furthermore, the elements of $\mathbf{1} \in \mathbf{R}^{1\times q}$ are all 1 and $\gamma > 0$. The term in (2) with γ is a penalty to approximately enforce the constraint $\sum_k h_b[k] = 1$ which ensures that the DC gain of H_b is close to 1. This is important because h_b is in series with h_f and so it should preserve the magnitude and phase properties of h_f below the high-pass corner frequency. Recall that h_b is designed so that only the high-frequency range of the feedthrough is modified with this filter –it is still necessary for h_f to provide effective feedthrough cancellation at lower frequencies, where the demarcation between high and low frequencies is the corner frequency of the high-pass filter H_{hp}.

The experimental results are reported when $q = 20$ with the values of the taps of h_b determined from (2) shown in Fig. 6. The high-pass filters are 4-pole discrete-time filters with corner frequencies equal to 2.5kHz. Thus, the bootstrap feedforward filter attempts to match any residual feedthrough in $\tilde{y}$ beyond 2.5 kHz that is not captured by h_f. The empirical frequency response when both feedforward filters are used is shown in Fig. 9 and illustrates that significant improvement in the high frequency suppression of the plant feedthrough is achieved. The feedforward compensated plant now allows for the implementation of a more aggressive controller possessing greater phase

lead and larger low frequency gain. The updated controller is denoted K_2 in Fig. 8 and the corresponding input sensitivity function is labeled S_2 in Fig. 10.

5. Discussion

A feedforward filter based on identifying a feedthrough model from open-loop testing is adequate for stabilizing the system, however, the closed-loop disturbance rejection properties are quite poor as evidenced by the large peak in the input sensitivity function S_1 in Fig. 10. This is caused by the high frequency limits placed on the controller gain due to imperfect feedthrough cancellation in the stabilized system. Suppressing residual feedthrough at higher frequencies by adding additional low-pass filtering in the controller will erode the phase-lead that is necessary for stabilizing the plant and therefore is not a viable approach for dealing with the partial cancellation afforded by h_f. Indeed, the feedthrough is a function of the beam angle and so it is necessary to identify the feedthrough about the nominal beam angle when the beam is stabilized. The bootstrap feedforward filter augments the initial feedforward filter to improve the high-frequency cancellation. Better matching of the feedthrough is obtained by testing the closed-loop system operating about the stabilized beam position and, once the correction to the initial feedthrough filter is determined and implemented as the filter h_b placed in series with h_f, a controller with greater phase lead can be implemented. The result is a significant improvement in the input sensitivity function (S_2 in Fig. 10). The Nyquist plot of the loop gain $(P - H_bH_f)K_2$ containing both feedforward filters is shown in Fig. 11. Since the plant is open-loop unstable with one unstable pole, the single necessary counterclockwise encirclement of $-1 + j0$ for closed-loop stability is evident in this figure. Removing the bootstrap feedforward filter (i.e., setting $H_b = 1$), however, produces an unstable closed-loop system with K_2.

The desirable sensitivity properties of S_2 in Fig. 10 only address uncertainty associated with the compensated plant $P - H_bH_f$. In order to determine the sensitivity to mismatch between the feedforward filters and the plant feedthrough, it is necessary to study another closed-loop transfer function. A perturbation at the output of P is shown as the block Δ in Fig. 5. This perturbation captures deviations between the plant feedthrough and the feedforward filters. When the initial feedforward filter H_f is used with controller K_1,

$$y/w = \frac{-PK_1}{1 + (P - H_f)K_1}.$$

Similarly, when both feedforward filters are used with controller K_2, then

$$y/w = \frac{-PK_2}{1 + (P - H_bH_f)K_2}.$$

The magnitudes of y/w for these cases are graphed in Fig. 12. They reveal that the stability of the closed-loop system is quite sensitive to uncertainty at the plant output, which is governed by the plant feedthrough. In fact, if good feedthrough cancellation is achieved, then $|(P - H_bH_f)K_2| << 1$ at high frequencies so

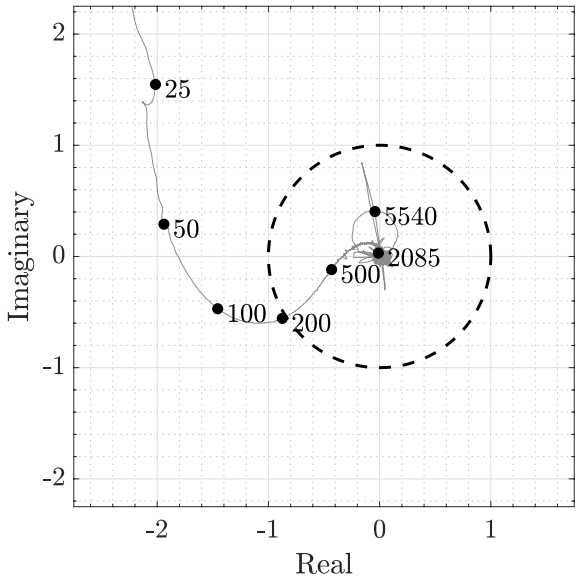

Figure 11: Nyquist plot of loop gain $(P - H_bH_f)K_2$. The closed-loop system is asymptotically stable. Frequency markers are given in Hertz.

$y/w \approx -PK_2$ at high frequencies. Thus, better cancellation in principle permits high-gain controllers, however, the closed-loop system becomes more sensitive to deviations between the actual feedthrough and the feedforward filters that are intended to cancel the feedthrough. This trade-off appears to be unavoidable if a more "traditional" sensitivity function like S_2 is desired. The alternative is to implement a controller that does not provide much performance beyond stabilizing the system.

It is reasonable to question whether using an electrode for both sensing and actuation is justified because of the complexity of identifying an accurate feedthrough model and then implementing an appropriate feedforward filter. The answer will depend on the application, but if the total electrode area is fixed, then segregating the sensing and actuation functions will lower the motional gain since less sensing area is available. This will reduce the signal-to-noise ratio of the measurement associated with the proof mass displacement. Furthermore, the actuation electrode potentials will increase for two reasons. First, the reduction in electrode area requires higher potentials to produce the same electrostatic forces, and, second, the electrostatic forces created by the sensing electrodes must now be overcome. These higher potentials are often a concern since dielectric breakdown is a risk with the small electrode-proof mass gaps. The sparking that can occur in the gaps can erode the electrodes and also damage the proof mass so it is desirable to reduce the electrode voltages to a minimum practical level, which is achieved by using the electrodes as both forcers and pick-offs.

6. Conclusion

Experimental results with a bootstrap feedforward compensation procedure to improve closed-loop disturbance rejection in an unstable 1-DOF system is reported. A process is developed

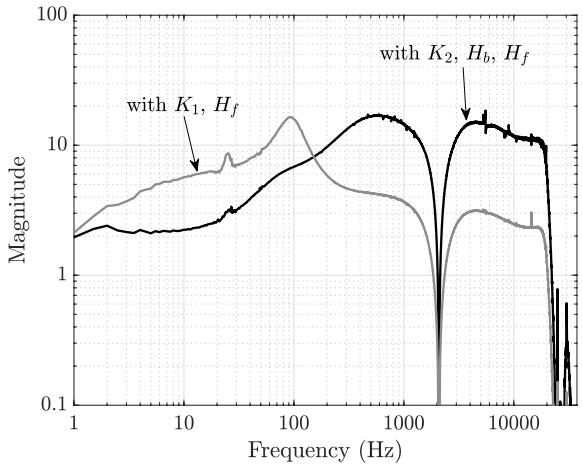

Figure 12: Frequency response of y/w illustrating the sensitivity of the closed-loop system to perturbations in the plant feedthrough.

to update a feedforward cancellation filter based on open-loop measurements with a bootstrap feedforward filter determined from testing the stabilized system. The improved suppression of the feedthrough allows for a controller with much larger gains and, consequently, the closed-loop sensitivity to disturbances at the plant input is reduced. A more aggressive controller requires precise matching between the feedforward filters and the plant feedthrough since the higher-gain controller amplifies any persisting differences. Thus, this approach is sensitive to deviations between the feedthrough and feedforward filters, however, the experimental results show that close matching is feasible in practice. Future directions will apply this feedforward compensation procedure to a multi-DOF electrostatic suspension system.

A methodology for generating a frequency response function associated with the linear-time periodic equations of motion is also described. This modeling technique is an extension of a previously reported approach introduced in [6], but it has the benefit of extending the frequency range to the Nyquist frequency associated with the experiments whereas the models in [6] were limited to estimating the frequency response up to half of the carrier frequency ω_0. This extends the model frequency responses from the high-frequency limit of $12.5\,\text{kHz}$ in [6] to a limit of $37.5\,\text{kHz}$ in the present work. The approximate frequency responses procured with this technique show very good agreement with experimentally obtained frequency responses and appears to be a reasonable approach for generating a frequency response that is suitable for control design. Further analysis of this method will be the subject of future papers.

Acknowledgement: The authors thank the staff of the UCLA Nanoelectronics Research Facility. This research did not receive any specific grant from funding agencies in the public, commercial, or not-for-profit sectors.

Appendix A. Modeling Framework

The equations of motion for the transformer's voltages and currents are consolidated into the following state-space description,

$$M(\theta)\dot{x} = Ax + B_1 i_{ct} + B_2 v_c \tag{A.1}$$

where the mass matrix $M(\theta) \in \mathbf{R}^{19\times 19}$ is dependent on the beam angle θ, $x \in \mathbf{R}^{19}$ is a vector of currents and voltages, and the matrices A, B_1, and B_2 are determined by the current-voltage relationships as derived via Kirchhoff's Laws (see [6]). The beam equations of motion are

$$\frac{d}{dt}\begin{bmatrix}\theta\\ \dot{\theta}\end{bmatrix} = \begin{bmatrix}\dot{\theta}\\ f(\theta;x)\end{bmatrix} \tag{A.2}$$

where

$$f(\theta;x) = \frac{L}{J}\frac{\epsilon A}{2}\left(-\underbrace{\frac{v_1^2}{(d_0+L\theta)^2}}_{F_1} + \underbrace{\frac{v_2^2}{(d_0-L\theta)^2}}_{F_2}\right)$$

is the moment applied to the beam normalized by the moment of inertia and θ represents the angle that the beam makes with respect to plane of the glass substrate and electrodes. Table A.1 lists the measured parameter values for the beam and transformer used in the analysis. Equations (A.1) and (A.2) are coupled through the voltages v_1 and v_2 and θ as described by the moment equation. The voltages v_1 and v_2 generate electrostatic forces on the beam and θ, conversely, dictates the capacitance developed between the electrodes and beam thereby affecting the electrode potentials. When $v_c = 0$ and $\theta(t) = 0$, the steady-state response of the circuit variables (A.1) are found via the frequency response of (A.1),

$$x_0(t) \stackrel{r}{=} \left(j2\pi\omega_0 M(0) - A\right)^{-1} B_1 a_{ct} e^{j2\pi\omega_0 t} \tag{A.3}$$

where $\stackrel{r}{=}$ denotes the extraction of the real part of the expression. In this solution, $v_1(t) = v_2(t)$ and therefore $f(0, x_0) = 0$. Collectively, x_0, $\theta(t) = 0$, and $\dot{\theta}(t) = 0$ represent a periodic solution in which the beam is stationary. The stability of this solution is analyzed by deriving the linear variational equations [8]. The perturbation variables are introduced as $x = x_0 + \delta_x$, $\theta = 0 + \delta_\theta$ and $\dot{\theta} = 0 + \delta_{\dot{\theta}}$. The control voltage is specified as $v_c = \delta_{v_c}\cos(\omega_0 t + \phi_c)$. Substituting these expressions into (A.1) and (A.2), linearizing $M(\theta)$ about $\theta = 0$, and retaining only linear terms yields the following variational equations,

$$\begin{aligned} M(0)\dot{\delta}_x &= A\delta_x - M_\theta \dot{x}_0 \delta_\theta + B_2\cos(2\pi\omega_0 t + \phi_c)\delta_{v_c}\\ \frac{d}{dt}\begin{bmatrix}\delta_\theta\\ \delta_{\dot{\theta}}\end{bmatrix} &= \begin{bmatrix}\delta_{\dot{\theta}}\\ f_\theta\delta_\theta + f_x\delta_x\end{bmatrix}, \end{aligned} \tag{A.4}$$

where $f_\theta := \frac{\partial f}{\partial\theta}(0;x_0)$ and $f_x := \nabla_x f(0;x_0)$ are the gradients of f with respect to θ and x evaluated on the periodic solution. These equations are time periodic with period $\tau_p = 1/\omega_0$ but are also overdetermined. The constraints are eliminated using a singular value decomposition of $M(0)$,

$$M(0) = \underbrace{\begin{bmatrix}U_1 & U_2\end{bmatrix}}_{U}\begin{bmatrix}\Sigma_1 & 0\\ 0 & 0\end{bmatrix}\underbrace{\begin{bmatrix}V_1^T\\ V_2^T\end{bmatrix}}_{V^T}$$

where U and V are unitary matrices, $U_1 \in \mathbf{R}^{19\times 6}$, $V_1 \in \mathbf{R}^{19\times 6}$, $\Sigma_1 \in \mathbf{R}^{6\times 6}$ is positive definite. New perturbation variables are defined according to

$$\delta_x = \begin{bmatrix} V_1 & V_2 \end{bmatrix} \begin{bmatrix} \delta_1 \\ \delta_2 \end{bmatrix}$$

where the dimensions of δ_1 and δ_2 are compatible with the partitioning of V. By substituting δ_x into (A.4), a set of differential equations and a set of algebraic constraints is produced:

$$\begin{aligned} \Sigma_1 \dot{\delta}_1 &= U_1^T A V_1 \delta_1 + U_1^T A V_2 \delta_2 - U_1^T M_\theta \dot{x}_0 \delta_\theta \\ &\quad + U_1^T B_2 \cos(2\pi\omega_0 t + \phi_{v_c}) \delta_{v_c} \\ 0 &= U_2^T A V_1 \delta_1 + U_2^T A V_2 \delta_2 - U_2^T M_\theta \dot{x}_0 \delta_\theta \\ &\quad + U_2^T B_2 \cos(2\pi\omega_0 t + \phi_{v_c}) \delta_{v_c} \end{aligned},$$

where $U_2^T A V_2$ is invertible so δ_2 can be expressed in terms of δ_1, δ_θ and δ_{v_c}. To simplify ensuing expression, the matrix $P \in \mathbf{R}^{19\times 19}$ is defined to be $V_2 \left(U_2^T A V_2\right)^{-1} U_2^T$. Additionally, the dynamics of the Butterworth filters H_s and H_a are respectively modeled by the linear systems $(A_s, B_s, C_s, 0)$ and $(A_a, B_a, C_a, 0)$ with the state vectors $\delta_s \in \mathbf{R}^4$ and $\delta_a \in \mathbf{R}^8$, the vector length corresponding to the order of the filter. Furthermore, the output of the smoothing filter is a_c and with respect to the control voltage perturbation, $\delta_{v_c} = C_s \delta_s$. These filter states are decoupled from those governing the transformer-beam system and, consequently, are invariant to the coordinate transformation set forth by the SVD of $M(0)$. After eliminating δ_2, the linear time-periodic differential equations reduce to

$$\begin{aligned} \dot{\delta}_s &= A_s \delta_s + B_s u \\ \dot{\delta}_1 &= \Sigma_1^{-1} U_1^T \left(I - AP\right) \left[A V_1 \delta_1 - M_\theta \dot{x}_0 \delta_\theta \right. \\ &\qquad \left. + B_2 \cos(2\pi\omega_0 t + \phi_c) C_s \delta_s\right], \\ \dot{\delta}_\theta &= \delta_{\dot{\theta}}, \\ \dot{\delta}_{\dot{\theta}} &= \left(f_\theta + f_x P M_\theta \dot{x}_0\right) \delta_\theta + f_x \left(I - PA\right) V_1 \delta_1 \\ &\qquad - f_x P B_2 \cos(2\pi\omega_0 t + \phi_c) C_{sm} \delta_{sm} \\ \dot{\delta}_a &= A_a \delta_a + B_a v_s \cos(2\pi\omega_0 t + \phi_s) \\ y &= C_a \delta_a. \end{aligned} \tag{A.5}$$

Note that v_s in the δ_a ODE can be expressed in terms of δ_1. These equations are consolidated into a 20-state system with state vector δ,

$$\delta = \left[\delta_s,\ \delta_1,\ \delta_\theta,\ \delta_{\dot{\theta}},\ \delta_a\right],$$

input u, output y, and state-space matrices $A_\delta(t)$, $B_\delta(t)$, and C_δ as shown in (1).

Appendix B. Frequency Response Analysis

An approximate frequency response associated with (1) can be derived. The key point is that the beam acts like a low-pass filter with regard to the rapidly varying electrostatic forces acting on it. The rapid variation is at twice the carrier frequency, i.e. $2\omega_0$. Thus, the beam essentially responds to the mean value of the forces. There is also additional band-limiting due to the smoothing and anti-alias filters. Under these conditions, it is possible to derive an approximate frequency response associated with a discrete-time system whose sample rate matches that of the controller. The approximate frequency response closely matches the motional and feedthrough measurements on the physical system reported in Section 4. Consider the solution of (1)

$$\delta(t) = \Phi(t, t_0)\delta(t_0) + \int_{t_0}^{t} \Phi(t, \tau) B_\delta(\tau) u(\tau) d\tau, \tag{B.1}$$

where $t \geq t_0$ and $\delta(t_0)$ is the initial condition. The controller sample rate is denoted ω_s (in hertz) and the corresponding sampling period is $t_s = 1/\omega_s$. The experiments in Section 4 employ a sample rate of $\omega_s = 3\omega_0$, so $t_s = \tau_p/3$. In other words, the controller sample rate is three times the carrier frequency. The analysis focuses on this case since it reflects the experimental conditions. It is also assumed that $t_0 = 0$.

First, consider u to be constant, which may be taken to be 1 without loss of generality because of the linearity of the differential equations. It is possible to find periodic solutions for all state variables because $\Phi(\tau_p, 0)$ does not have an eigenvalue equal to one. The states are periodic with period τ_p (may not be the minimal period) because it is possible to solve for $\delta(t)$ by enforcing $\delta(t + \tau_p) = \delta(t)$ in (B.1),

$$\delta(t) = \left(I - \Phi(t + \tau_p, t)\right)^{-1} \int_t^{t+\tau_p} \Phi(t + \tau_p, \tau) B_\delta(\tau) d\tau.$$

As t is varied over one period, say the interval $[0, \tau_p]$, the periodic solution of the state vector is obtained. When the beam angle deviation δ_θ is extracted from the state vector, it is discovered that the ratio of its peak-to-peak variation to its average value is less than 10^{-5} for the transformer-beam model in Fig. 1. In other words, for all practical purposes δ_θ can be taken to be constant. Nevertheless, further analysis shows that the beam angle is actually periodic with period $\tau_p/2$. This is not surprising because the electrostatic forces on the beam are proportional to the square of the electrode voltages, thus, with a constant control voltage, the time-varying portion of the electrostatic forces are sinusoids with twice the carrier frequency, i.e. $2\omega_0$. This demonstrates the beam acts like a low-pass filter as far as the amplitude modulated electrode voltages are concerned. This observation forms the basis of the approximate frequency response derivation proposed below.

The case when u is not constant is now analyzed. The DSP implements a zero-order-hold on the discrete-time control sequence so it is possible to integrate the equations of motion over one sample period t_s. Thus, define,

$$\begin{aligned} \Phi_k &= \Phi(kt_s, (k-1)t_s), \\ \Gamma_k &= \int_{(k-1)t_s}^{kt_s} \Phi(kt_s, t) B_\delta(t) dt, \quad k = 1, 2, 3. \end{aligned}$$

Consider a sequence $\{u_n\}$, $n \in \mathbb{Z}$, issued by the discrete-time controller. Define the sequence $\{\delta_n\}$ where $\delta_n = \delta(nt_s)$. It is

Transformer Parameters				Beam Parameters	
Parameter	**Value**	**Parameter**	**Value**	**Parameter**	**Value**
L_1, L_2	2.1 H	R_{21}	100 Ω	beam length	52 mm
L_s	1.53 mH	R_k	100 Ω	beam width	25 mm
L_x	2.47 μH	R_d	1 MΩ	beam thickness	500 μm
M_p	2.1 H	C_1	variable	electrode area, A	1.21 cm^2
M_s	57.68 mH	C_2	variable	dielectric constant, ϵ	8.85×10^{-12} F · m^{-1}
R_{11}	504 Ω	C_p	17 pF	fulcrum/electrode distance, L	1.45 cm
R_{12}	504 Ω	C_{i_1}	70 pF	nominal beam/electrode gap, d_0	10 μm
R_{22}	0.54 Ω	C_{i_2}	70 pF	moment of inertia, J	0.341×10^{-6} kg · m^2

Table A.1: Transformer passive component values and beam parameters.

evident

$$\begin{aligned}
\delta_{n+1} &= \Phi_1\delta_n + \Gamma_1 u_n \\
\delta_{n+2} &= \Phi_2\delta_{n+1} + \Gamma_2 u_{n+1} \\
\delta_{n+3} &= \Phi_3\delta_{n+2} + \Gamma_3 u_{n+2} \qquad \text{when } n \equiv 0 \,(\mathrm{mod}3) \\
\delta_{n+4} &= \Phi_1\delta_{n+3} + \Gamma_1 u_{n+3} \\
&\vdots
\end{aligned} \tag{B.2}$$

If $n \not\equiv 0 \,(\mathrm{mod}3)$ then there are permutations of Φ_k and Γ_k in the expressions for the samples of δ in (B.2) and this scenario corresponds to selecting $t_0 \in \{t_s, 2t_s\}$. The conclusions of the analysis do not change, though, for arbitrary t_0. Generally, sinusoidal solutions describing consecutive samples of δ_n do not exist for (B.2), however, because of the cyclic nature of the mappings, it is possible to relate every third sample with linear time-invariant expressions,

$$\begin{aligned}
\delta_{n+3} &= \Phi_3\Phi_2\Phi_1\delta_n + \Phi_3\Phi_2\Gamma_1 u_n \\
&\quad + \Phi_3\Gamma_2 u_{n+1} + \Gamma_3 u_{n+2} \\
\delta_{n+4} &= \Phi_1\Phi_3\Phi_2\delta_{n+1} + \Phi_1\Phi_3\Gamma_2 u_{n+1} \\
&\quad + \Phi_1\Gamma_3 u_{n+2} + \Gamma_1 u_{n+3} \qquad \text{when } n \equiv 0 \,(\mathrm{mod}3) \\
\delta_{n+5} &= \Phi_2\Phi_1\Phi_3\delta_{n+2} + \Phi_2\Phi_1\Gamma_3 u_{n+2} \\
&\quad + \Phi_2\Gamma_1 u_{n+3} + \Gamma_2 u_{n+4}
\end{aligned} \tag{B.3}$$

The notion of a frequency response function is developed by assuming the input sequence is sinusoidal, in other words, $u_n = e^{j2\pi\omega n t_s}$, and that $\delta_n = \hat{\delta}_0 e^{j2\pi\omega n t_s}$, $\delta_{n+1} = \hat{\delta}_1 e^{j2\pi\omega(n+1)t_s}$, and $\delta_{n+2} = \hat{\delta}_2 e^{j2\pi\omega(n+2)t_s}$, where $\hat{\delta}_0$, $\hat{\delta}_1$, and $\hat{\delta}_2$ are to be determined. Substituting these sinusoids into (B.3) and noting $\delta_{n+3} = \hat{\delta}_0 e^{j2\pi\omega\tau_p} e^{j2\pi\omega n t_s}$, $\delta_{n+4} = \hat{\delta}_1 e^{j2\pi\omega\tau_p} e^{j2\pi\omega(n+1)t_s}$ and $\delta_{n+5} = \hat{\delta}_2 e^{j2\pi\omega\tau_p} e^{j2\pi\omega(n+2)t_s}$ yields the following expressions,

$$\begin{aligned}
\hat{\delta}_0 &:= \left(e^{j2\pi\omega\tau_p} I - \Phi_3\Phi_2\Phi_1\right)^{-1} \tilde{\Gamma}_1 \\
\hat{\delta}_1 &:= \left(e^{j2\pi\omega\tau_p} I - \Phi_1\Phi_3\Phi_2\right)^{-1} \tilde{\Gamma}_2 \\
\hat{\delta}_2 &:= \left(e^{j2\pi\omega\tau_p} I - \Phi_2\Phi_1\Phi_3\right)^{-1} \tilde{\Gamma}_3,
\end{aligned} \tag{B.4}$$

where

$$\begin{aligned}
\tilde{\Gamma}_1 &:= \Phi_3\Phi_2\Gamma_1 + \Phi_3\Gamma_2 e^{j2\pi\omega t_s} + \Gamma_3 e^{j4\pi\omega t_s} \\
\tilde{\Gamma}_2 &:= \Phi_1\Phi_3\Gamma_2 + \Phi_1\Gamma_3 e^{j2\pi\omega t_s} + \Gamma_1 e^{j4\pi\omega t_s} \\
\tilde{\Gamma}_3 &:= \Phi_2\Phi_1\Gamma_3 + \Phi_2\Gamma_1 e^{j2\pi\omega t_s} + \Gamma_2 e^{j4\pi\omega t_s}
\end{aligned} \tag{B.5}$$

This reveals that every third sample can in fact be expressed in "frequency response" form, however, consecutive samples generally cannot be expressed in this manner. Despite this fact, any rapidly varying electrostatic forces on the beam over one period of the carrier can be assumed to produce an *average* effect due to the filtering by the beam inertia. Thus, the beam motion, and by extension the output voltage y which represents a superposition of the beam motion with the feedthrough, can be approximated by the *average* of (B.4). In other words, the "frequency response" of the system is taken to be

$$y/u = \frac{1}{3} C_\delta \left(\hat{\delta}_0 + \hat{\delta}_1 + \hat{\delta}_2\right). \tag{B.6}$$

This expression is used to compute an approximate frequency response for the transformer-beam system from the perspective of the discrete-time controller. The frequency range extends to the Nyquist frequency associated with the controller sample rate, i.e. 37.5 kHz.

References

[1] J. L. Atkinson, "Electrostatic bearing," U.S. Patent 3,334,949, 1967.

[2] A. H. Behbahani, D. Kim, P. Stupar, J. DeNatale, and R. T. M'Closkey, "Tailored etch profiles for wafer-level frequency tuning of axisymmetric resonators," *J. Microelectromech. Syst.*, vol. 26, no. 2, pp. 333–343, April 2017.

[3] V. Josselin, P. Touboul, and R. Kielbasa, "Capacitive detection scheme for space accelerometers applications," *Sensors and Actuators A: Physical*, vol. 78, no. 2–3, pp. 92 – 98, 1999.

[4] R. Toda, N. Takeda, T. Murakoshi, S. Nakamura, and M. Esashi, "Electrostatically levitated spherical 3-axis accelerometer," in *The Fifteenth IEEE Int. Conf. Micro Electro Mech. Syst.* IEEE, Jan 2002, pp. 710–713.

[5] F. T. Han, Z. Gao, and Y. Wang, "A differential capacitance to voltage converter for electrostatic levitation applications," *Sensors and Actuators A: Physical*, vol. 99, no. 3, pp. 249 – 255, 2002.

[6] M. Andonian and R. T. M'Closkey, "Sensing and control interface for precise gap control," *Mechatronics*, vol. 56, pp. 277 – 286, 2018.

[7] J. C. Doyle, B. A. Francis, and A. R. Tannenbaum, *Feedback Control Theory*. New Jersey: Prentice Hall, 1991.

[8] J. K. Hale, *Oscillations in nonlinear systems*. New York: McGraw-Hill Book Company, Inc., 1963.